Geochemistry, Geophysics, Geosystems®

AGU ADVANCING EARTH AND SPACE SCIENCE

RESEARCH ARTICLE
10.1029/2022GC010765

Evidence of Fluid Induced Earthquake Swarms From High Resolution Earthquake Relocation in the Main Ethiopian Rift

Martina Raggiunti[1,2], Derek Keir[1,3], Carolina Pagli[2], and Aude Lavayssière[3,4]

[1]University of Florence, Firenze, Italy, [2]University of Pisa, Pisa, Italy, [3]University of Southampton, Southampton, UK, [4]Geo-Ocean, Univ Brest, CNRS, Ifremer, UMR6538, Plouzane, France

Key Points:

- Cross correlation and high-resolution relocation are used to investigate driving mechanisms of seismicity during continental rifting
- Earthquake relocation aligns seismicity to *N*–NNE striking, ~60° dipping planes corresponding to rift normal faults
- The cross-correlation analysis identifies similar earthquakes that occur in swarms in the rift, pointing toward them being fluid induced

Supporting Information:

Supporting Information may be found in the online version of this article.

Correspondence to:

M. Raggiunti,
martina.raggiunti@unifi.it

Citation:

Raggiunti, M., Keir, D., Pagli, C., & Lavayssière, A. (2023). Evidence of fluid induced earthquake swarms from high resolution earthquake relocation in the Main Ethiopian Rift. *Geochemistry, Geophysics, Geosystems*, *24*, e2022GC010765. https://doi.org/10.1029/2022GC010765

Received 31 OCT 2022
Accepted 17 MAR 2023

Abstract Fluid overpressure and fluid migration are known to be able to trigger or induce fault slip. However, relatively little is known about the role of fluids on generating earthquakes in some of the major continental rifts. To address this, we investigate the interaction between fluids and faults in the Main Ethiopian Rift (MER) using a large seismicity catalog that covers both the rift axis and rift margin. We performed cross-correlation analysis on four major earthquake clusters (three within the rift and one on the rift margin) in order to significantly improve accuracy of the earthquake relative relocations and to quantify families of earthquakes in which waveforms are similar. We also analyzed variation of seismicity rate and seismic moment release through time for the four clusters. The major results are that for all four clusters the earthquake relocations are 5–15 km deep, aligned to clear N-NNE striking, steeply (>60°) dipping planes. For the three clusters within the rift, the cross-correlation analysis identifies earthquake families that occur in short swarms during which seismic rate and moment release increases. Together, this space and time pattern of the seismicity strongly points toward them being fluid induced, with fluid likely sourced from depth such as mantle derived CO_2. In contrast, the seismicity on the rift margin lacks earthquake families, with occurrence of earthquakes more continuous in nature, which we interpret as pointing toward tectonic stress-driven microseismic creep. Overall, our results suggest that deep sourced fluid migration within the rift is an important driver of earthquake activity.

Plain Language Summary Fluids such as water and carbon dioxide that come from the deep Earth can move toward the surface by following fractures and faults. When this happens, these fluids make it easier for the faults to move, causing lots of small earthquakes to happen in short periods of time and in the same place. These earthquake swarms have typical characteristics such as waveforms that are incredibly similar to each other. In our study, we are interested in understanding how important the movement of fluids is for the generation of earthquakes during the breakup of continents. We investigated the presence of these characteristics for earthquakes in the Main Ethiopian Rift in East Africa. Major findings are that earthquake swarms within the rift have characteristics that indicate earthquakes are generated by fluid flow along faults. In contrast at the edges of the rift, the earthquakes are different in character, which indicates that they are caused by tectonic motion of the plates rather than fluid migration.

1. Introduction

Fluids and their migration can influence faulting in various ways, primarily by modifying the state of crustal stresses and hence affecting the nucleation, propagation, and arrest of earthquakes (Hickman et al., 1995; Sibson, 2000; Yamashita & Tsutsumi, 2018). Fluids can modify the elastic parameters of rocks, as an increase in the pore fluid pressure causes an increase of the Poisson's ratio and a decrease in P- and S- wave velocities (Christensen, 1984). Fluids can also control whether a fault zone behaves in a stick-slip or continuous creep fashion (Yamashita & Tsutsumi, 2018).

The most common fluids in the crust are H_2O and CO_2, which can have a range of origins such as from dehydration of minerals, from magma degassing or simply as fluids trapped in pore spaces, or from percolation of meteoric water (Hickman et al., 1995). In particular, the presence of CO_2 in rifts from magma degassing has been shown to be of potential global significance (Brune et al., 2017). The CO_2 from the mantle can migrate upward as magma ascends through the lithosphere, decompresses, and starts crystallizing and exsolving volatiles, which can then reach the surface through faults and fractures (Lee et al., 2016).

Fluid induced earthquakes have characteristics that differ from stress-driven earthquakes. They typically occur in sequences of events without a single dominant shock, with a rate of seismicity which fluctuates in time and does not follow Omori's law (1894) (Fischer et al., 2014; Ruch et al., 2021; Shcherbakov et al., 2004). Other common characteristics of fluid induced earthquakes include spatial migration of the hypocenters through time, tensile fault slip, events of outflow of groundwater and gases, and seismic activity triggered from distant earthquakes (Yamashita & Tsutsumi, 2018). Fluid induced earthquake sequences are also commonly characterized by significant waveform similarity at the recording station. This happens because the earthquakes in the swarm share similar source mechanisms, locations, ray path and site response (Lindenfeld et al., 2012).

In this work, the time and space patterns of seismicity beneath the Ethiopian rift are investigated in detail in order to understand whether they are likely associated with fluids or not. More specifically, we focused on the northern sector of Main Ethiopian Rift (MER) where the Ankober border fault of the rift margin, and the Fentale Dofen (FD) magmatic segment in the rift valley floor have been highly active seismically (Keir et al., 2006; Temtime et al., 2020). First, we significantly improved on the accuracy of earthquake locations by using relative earthquake relocation following waveform cross correlation. Then, we analyzed the degree of waveform similarity combined with the space-time pattern of the seismicity. This allowed us to identify families of similar earthquakes in the FD magmatic segment that happened in spatially and temporally isolated swarms, during which seismicity rate and moment release increase. In contrast, we find that the seismicity on the Ankober border fault lacks distinct earthquake families. Overall, we interpret that seismicity in the FD magmatic segment is being likely induced by fluid migration, whereas seismicity on the Ankober border fault to be less related to fluid processes.

2. Tectonic Setting

The MER is a NE trending sector at the northern end of the East African rift system (Bonini et al., 2005). The MER extends from the Turkana depression to the Afar depression, where it intersects the Red Sea and the Gulf of Aden producing a triple junction between the Nubian, Arabian, and Somalian plates (Corti, 2009; Ebinger & Casey, 2001; Wolfenden et al., 2005). The rift is an intracontinental extensional system that records the transition from continental rifting to seafloor spreading (Abebe et al., 2007; Chorowicz, 2005; Ebinger & Casey, 2001). The MER shows a typical rift morphology, characterized by an ~80 km-wide rift valley that separates the Ethiopian plateau on the western side and the Somalian plateau on the eastern side.

The rift can be subdivided into three main sectors that have along-rift changes in rift orientation (Agostini et al., 2011) and degree of magmatism (Keir et al., 2015) and potentially reflect different stages of rift development (Keranen & Klemperer, 2008). The Northern MER (NMER) is thought to have initiated at around 10–11 Ma and has main boundary faults that strike ~*N*50° on the eastern side of the rift (Agostini et al., 2011). The orientation of the NMER border faults on the western side changes northward from ~*N*50° to near *N*–*S* due to the MER linking with the border faults of the western Afar margin (Wolfenden et al., 2005). The structural boundary Boru Toru Structural High separates the NMER from the Central MER (CMER). The CMER is thought to have initiated around 8.3–9.7 Ma and the rift border faults are oriented *N*30°–*N*35° (Bonini et al., 2005). The Southern MER (SMER) starts south of the Goba-Bonga transverse lineament (Bonini et al., 2005; Corti, 2009). Rifting in this sector initiated between 18 and 21 Ma, and the rift border faults range from *N*–*S* to *N*20° in strike (Bonini et al., 2005).

The MER is characterized by active extensional tectonics that accommodate the relative movement between the Nubian plate (Ethiopian plateau) and Somalian plate (Somalian plateau) (Bonini et al., 2005). The distribution of extension has changed through time. Initially the strain is thought to have been accommodated by the border faults that delimit the rift (Wolfenden et al., 2005). However structural and stratigraphic data indicate that from 2.5 Ma the extensional strain has migrated from the border faults to <20 km-wide zones in the rift valley floor known as "Quaternary-Recent magmatic segments" which include dense networks of small offset faults known as the Wonji Fault Belt, aligned with Quaternary to Recent eruptive centers and lava flows (Boccaletti et al., 1999; Maguire et al., 2006; Wolfenden et al., 2005). Geodetic data suggest that the magmatic segments currently accommodate more than 50% of the extensional strain (Birhanu et al., 2016), with most of the Quaternary-Recent volcanism also occurring within them (Siegburg et al., 2020). A range of approaches have been used to constrain the rate and the direction of this movement, such as inversion of earthquake focal mechanisms (Keir et al., 2006; Lavayssière, Drooff, et al., 2019), GPS measurement (Birhanu et al., 2016; Fernandes et al., 2004; Kogan et al., 2012), plate kinematic reconstruction (Chu & Gordon, 1999), and structural geology

(Corti et al., 2020; Wolfenden et al., 2004). The results of these are generally consistent and reveal an average extension rate of 5–7 mm/y with a ~*N*85°–105°E direction.

The MER is seismically active with insights provided by earthquake catalogs from both permanent global stations, and from high density, temporary seismic networks. The early studies of earthquake activity in the MER relied on recordings of larger ($M > 3.5$) earthquakes on permanent, global stations (Ayele, 1995; Ayele & Kulhánek, 1997; Hofstetter & Beyth, 2003). These studies identified a transition from broadly distributed seismicity in the SMER, to more focused rift axial seismicity in the NMER, as well as the dominantly mid to upper crustal depth of earthquakes through the region. Hofstetter and Beyth (2003) also identified that the seismic moment release in the MER is far less than expected from the geodetically determined plate motions, tentatively suggesting that aseismic deformation such as dike intrusion or fluid induced fault creep may be important. Building on these studies, a number of dense, temporary seismic networks have operated in Ethiopia. The EAGLE study constrained seismicity in the CMER and NMER and concluded that the seismicity within the rift is mainly localized to the magmatic segments and also on the Ankober border fault on the western side of the MER—Afar intersection (Keir et al., 2006). The seismicity in these zones was characterized by low-magnitude swarms above ~15–18 km depth. The earthquake focal mechanisms are predominantly normal dip slip with fault planes striking from *N* to NNE. More recently, a number of dense, temporary seismic deployments have targeted specific volcanic centers such as Corbetti (Lavayssière, Greenfield, et al., 2019), Tulu Moye (Greenfield et al., 2019b), and Aluto (Wilks et al., 2017). A common feature of these studies managed to detect very shallow earthquakes in the upper 4 km of the crust beneath the volcanic centers. The swarm-like nature of these events in association with along and across rift fault networks were used to argue that very shallow seismicity is driven by hydrothermal fluid circulation concentrated along faults. Seismic experiments have also constrained crustal structure and show complexity in the crustal geometry related to extension. Crustal thickness is largest under the uplifted plateau regions, where it reaches 40–50 km thick (Mackenzie et al., 2005). Beneath the MER, the thickness of the crust decreases gradually northward from ~38 km beneath the CMER to ~24 km beneath Fentale volcano in the NMER (Mackenzie et al., 2005).

This work is focused on the NMER, especially around the rift sector including the FD magmatic segment, located between the Adama basin and Kereyou basin (red segment in Figure 1), and the adjacent Ankober border fault. The FD magmatic segment is a half-graben bounded by faults with 60–80 m high scarps on the eastern flank (Casey et al., 2006). It is characterized by intense seismic activity (Keir et al., 2006), as well as the presence of hydrothermal and fumarolic activity and numerous hot springs (Mohr & Gouin, 1976; Pürschel et al., 2013; Raggiunti et al., 2021; Wolfenden et al., 2004). The segment includes two main Quaternary-Recent volcanoes: the Dofan volcanic complex (DVC) and the Fentale volcano (Wolfenden et al., 2004). The DVC is a ~50 km^2 shield volcano WNW − ESE elongated. The morphology of the DVC is characterized by a series of subparallel, ~10 km-long, NNE − SSW striking faults with scarps that range from few tens to ~300 m that cut the volcanic complex. In the central sector of the complex the faults create a ~NNE − SSW striking graben while across the rift there is a WNW − ESE alignment of craters and cones (Raggiunti et al., 2021). The second volcano in the magmatic segment is Fentale volcano. The morphology of Fentale is dominated by a summit caldera with an elliptical shape ~3.5 km wide, 300 m deep and elongated WNW − ESE (Maestrelli et al., 2021; Raggiunti et al., 2021). The southern portion of the Fentale caldera is cut by a series of NNE − SSW striking extensional fissures, associated with, and parallel to, the major fault system, the Wonji Fault Belt (Williams et al., 2004). The Fentale volcano has intense fumarolic activity that has been interpreted as evidence of a shallow magma chamber (Teklemariam & Kebede, 2010).

3. Data

The seismic database used in this work was acquired from the seismic stations installed in the MER during project EAGLE (Ethiopia Geoscientific Lithospheric Experiment) during 2001–2003 (Figure 1 and Supporting Information S1) (Maguire, 2001; Maguire et al., 2003). The earthquake catalog consists of 2163 earthquakes, located using 13388 of P- and 12696 S- phase arrival times. The catalog uses three temporary networks, which was initially EAGLE Phase I with up to 29 broadband station with Güralp CMG-3T and CMG-40TD instruments recording at 50 samples per second for a period of 16 months from 2001 late October to 2003 January. EAGLE Phase II added 50 CMG-6TD instruments recording at 100 samples per second for a period of 4 months between 2002 November and 2003 February. In the end, the EAGLE Phase III controlled source profiles included

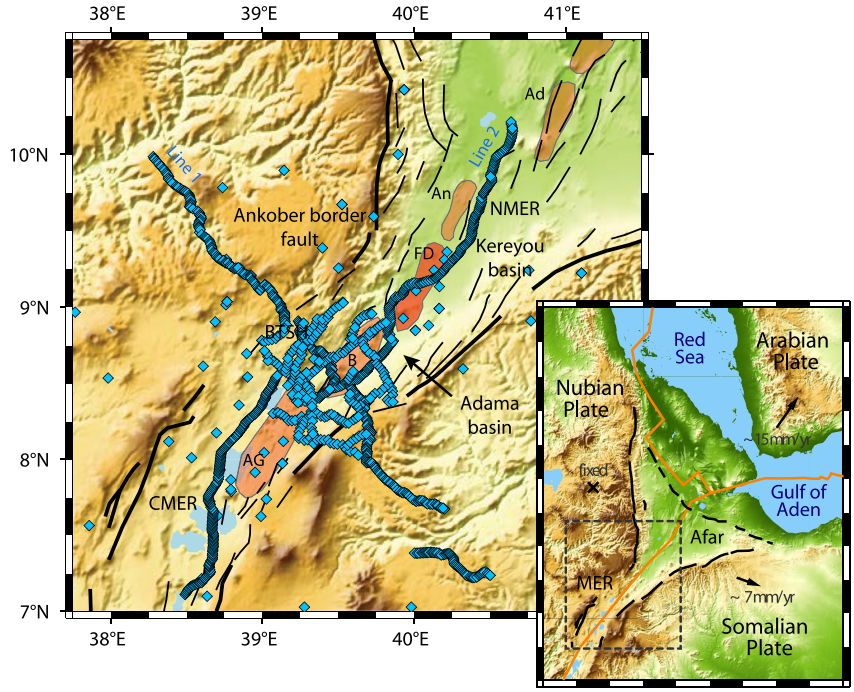

Figure 1. Tectonic setting of the area. In the image on the right are reported the border faults with black solid lines and the plate boundaries with the orange solid line. Dashed square corresponds to the area in the image on the left. BTSH indicates the Boru Toru Structural High separating the Northern Main Ethiopian Rift (MER) (NMER) from the Central MER (CMER). Light blue diamonds indicate the seismic station of the EAGLE project and in red are the magmatic segments: Aluto-Gedemsa magmatic segment (AG), Boset magmatic segment (b), Fentale-Dofan magmatic segment (Fentale Dofen (FD)), Angelele magmatic segment (An), and Addo-do magmatic segment (Ad). We focus on Fentale-Dofan magmatic segment FD.

the deployment of 91 Güralp CMG-6TD broad-band seismometers recording at 100 samples per second. The total period covered by the project is from October 2001 to February 2003. The original earthquake catalog is presented in Keir et al. (2006) and available in Data Set S2, and the waveforms available at IRIS Data Management Center (https://www.fdsn.org/networks/) under networks codes XJ, XM, and YJ. We analyzed the waveforms using Seismic Analysis Code format.

4. Methods

4.1. Appraisal of Earthquake Locations and Size Distribution

Using the phase arrivals, station locations and a reproduction of the 3D velocity model (Supporting Information S1) proposed by Maguire et al. (2006) based on the EAGLE Line 1, along-rift controlled source profile (Figure 1), the 2163 earthquakes are relocated in the MER using NonLinLoc Software (Lomax, 2008). Of these earthquakes, 1515 are located on or in proximity to the FD magmatic segment and the adjacent border fault (Figure 2). The earthquakes in the study area are divided into four main clusters based on visual inspection of the spatial distribution on map and in section of the events. The clusters 1, 2, and 3 are located in the rift and cluster 4 is located on the Ankober border faults (Figure 2).

The location method used in NonLinLoc involves a nonlinear relationship between hypocenter location and travel times, and the solution includes the uncertainties due to the spatial relation between network and event, measurement uncertainty in the observed travel times, and errors in the computation of theoretical travel times. The locations achieved using NonLinLoc are influenced by the velocity model, and its appropriateness and parameterization (Lomax et al., 2000, 2009) influences the location of the hypocenters. An indicator of the quality of location is the root-mean square travel-time residual (RMS), which can be defined as the best estimate of an origin time error in NonLinLoc. In our case, the mean value of RMS of the whole catalog is 0.36 s. The average error in latitude is ±5.84 km and ±5.63 km in longitude. The average error in depth is ±4.78 km.

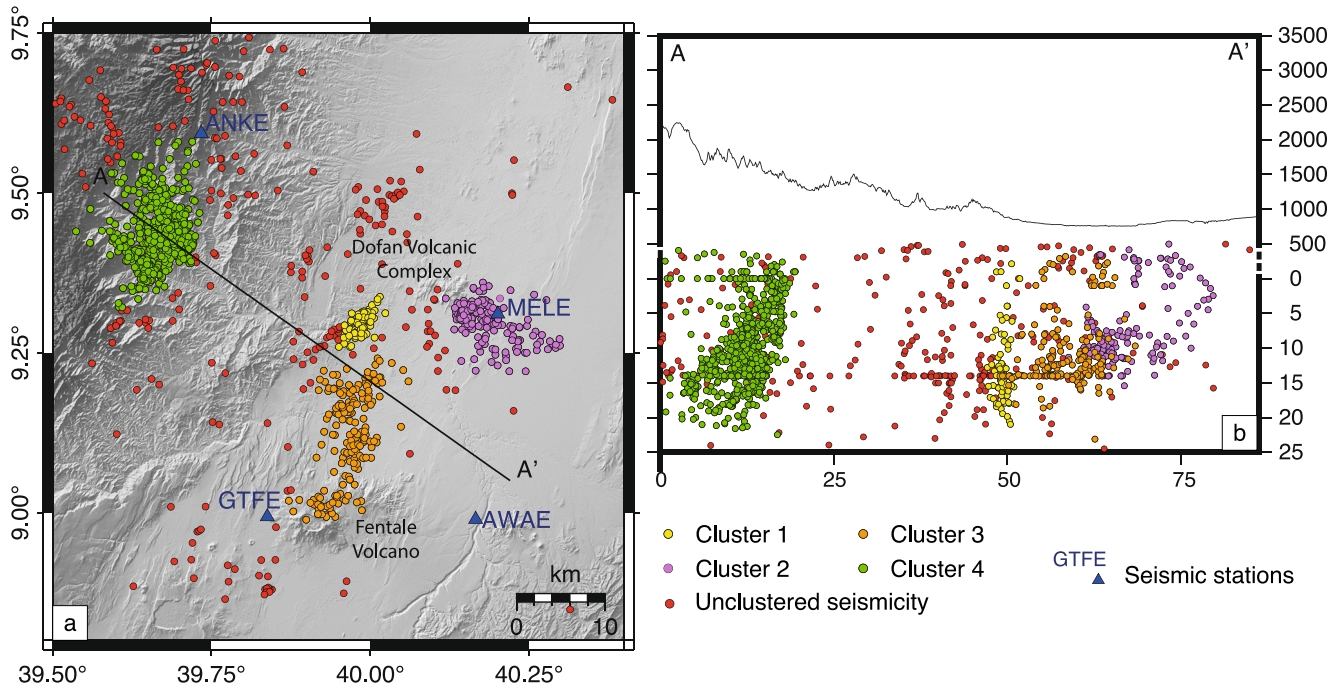

Figure 2. Seismic setting of the Fentale Dofen magmatic segment in (a) map and (b) cross section view. (a) Dofan volcanic complex = Dofan magmatic segment, FV = Fentale volcano. In blue there are the names of the seismic stations. The earthquakes are grouped in four clusters: cluster 1 yellow dots, cluster 2 purple dots, cluster 3 orange dots and cluster 4 green dots. The remaining scattered (unclustered) seismicity is shown as red dots. The black line is the cross section shown in panel (b).

The earthquake locations from NonLinLoc were merged with the original local magnitudes ML by Keir et al. (2006), obtaining a new catalog with updated locations. The magnitude values range from −0.23 to 4.33 with an average value of 1.64. We used the new catalog to compute the seismic moment using the equation by Bormann et al. (2002):

$$M_w = 2/3(\log M_0 - 9.1) \quad (1)$$

where M_0 is the seismic moment in Nm and M_w is the moment magnitude. We derived M_w by using the computed ML. This assumption is reasonable because both forms of magnitude refer to basic properties of the earthquake source, with global comparative studies showing empirically that at the low end of the magnitude scale the M_L and M_w have an average 1 to 1 relationship (Deichmann, 2006). We then computed the seismic moment release through time on a cluster by cluster basis.

4.2. Waveform Cross Correlation

Seismic waveforms produced by different earthquakes can have strong similarity, and the level of this similarity can be measured through waveform correlation (Dodge & Walter, 2015; Schaff, 2008) (Figure 3). In addition to being able to measure the similarity between the waveforms, the correlation can be also used to estimate the time delay that separates them, as long as the waveforms are similar enough (Campillo & Roux, 2015) (Figure 4). A high degree of correlation between seismograms from different events implies that these events have a similar source location and focal mechanism (Dodge & Walter, 2015). For this reason, cross correlation techniques have found application in many fields of seismology such as identification of repeating events, detection of lower magnitude events using waveform template matching (Saccorotti et al., 2022), and improving hypocentral locations (Schaff, 2008). Using the cross correlation approach in conjunction with the original arrival time phases, the earthquake location can be improved with respect to traditional methods (Schaff et al., 2018).

The cross correlation method is used here to both relocate the earthquakes and to understand whether families of similar waveforms exist in our earthquake catalog. We repicked the P-waves applying a 1–10 Hz band-pass filter, and for each pair of earthquakes recorded at each station we performed the cross correlation analysis using

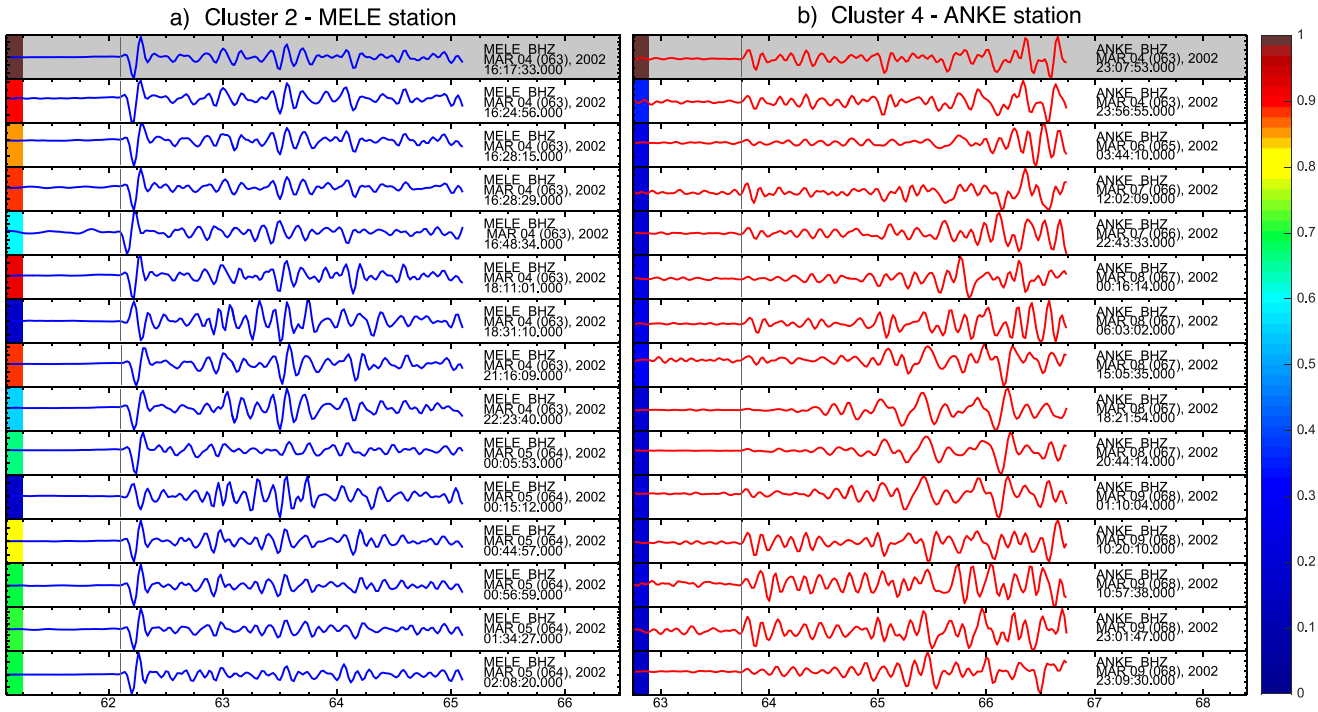

Figure 3. Example of waveforms compared in the cross correlation. (a) Earthquakes in the rift, cluster 2—MELE station and (b) earthquakes on the border fault, cluster 4—ANKE station. The waveforms in the top row, in gray shading, are compared with themselves and the following ones for each station. Cross correlation coefficient of each waveform compared to the one in the top row is shown as colored rectangle on the left-hand side of the panels. The cross correlation coefficient color bar is on the right side of the figure and it applies to both panels.

GISMO Software (Thompson et al., 2017). To perform the cross correlation, we arranged waveforms on a station by station basis and aligned the waveforms on the P-wave arrival. Then, we selected the part of the waveform from 10 s before the P wave arrival to 60 s after the P wave arrival. This time window was selected as it extracts the significant part of the seismic signal while reducing the computational time of the cross correlation. Noisy

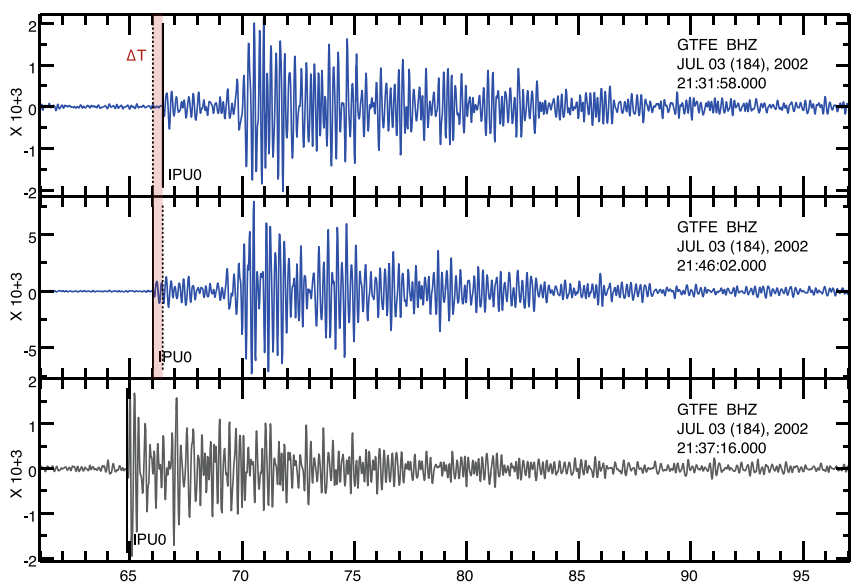

Figure 4. Example of correlation and differential time ΔT computation. Each panel shows a different earthquake recorded at the station GTFE on the vertical component. Between the blue waveforms there is a high level of correlation and it is possible to estimate the differential time ΔT. The gray waveform does not show similarity with the other two waveforms.

waveforms where the P-arrival was difficult to identify were discarded. Figure 3 shows an example of waveforms used in the cross correlation for earthquakes in the rift (left) and on the border faults (right) from the same few-day period. It is evident there is a higher level of similarity for the earthquakes localized within the rift. The analysis was performed separately for each of the four clusters since pairs of waveforms from different clusters do not correlate with each other. In this way one correlogram was produced for each station. Correlograms visually show the correlation coefficient for all pairs of earthquakes for each station in a cluster. This allows us to have a quantitative and visually appealing way of determining the presence of families of similar earthquake within the clusters, and their pattern in time.

4.3. Relative Earthquake Relocation

The effects of errors in earthquake location linked to the velocity model can be minimized using relative earthquake location methods that use the double-difference algorithm to compute the earthquake location (Waldhauser & Ellsworth, 2000). These location methods are based on the concept that the separation between two earthquakes is small compared to the event-station distance and the length scale of the velocity heterogeneity and the ray paths between source and common station are similar (Figure 4). Assuming this, the difference in travel times between two observed events is due to the spatial offset between the two events (Waldhauser & Ellsworth, 2000). To perform a double difference location, we used HypoDD software with a simple 1D velocity model, based on the velocity model by Maguire et al. (2006) (Supporting Information S1), composed of four planar layers (Supporting Information S1). The location with HypoDD was performed twice, the first was with only the catalog data (Supporting Information S1), and for the second, we added the cross correlation time of pairs of events with a coefficient of cross correlation equal or greater than 0.7, a value indicative of highly correlated waveforms and commonly used as a cutoff cross-correlation coefficient in earthquake relocation (Diehl et al., 2013; Waldhauser et al., 2012; Waldhauser & Schaff, 2008). Relative location uncertainty of the relocated events is difficult to quantify and relates to number of stations and number of earthquakes in the relocated clusters. Based on error estimates from previous studies (Got et al., 1994; Woods et al., 2019), coupled with our relative locations typically collapsing to distinct planes that project to surface faults, we estimate the horizontal and vertical errors are less than several hundred meters. The improvement in locations also results in a smaller average (0.19 s) and median (0.15 s) RMS. In Figure 5 are shown the histograms of RMS for the NonLinLoc catalog and for the events belonging to the four clusters relocalized with HypoDD.

5. Results

5.1. Initial Earthquake Locations and Size Distribution

The initial distribution of seismicity was obtained by locating P- and S- phase arrival times within the velocity model proposed by Maguire et al. (2006) (Supporting Information S1) and using NonLinLoc Software. The locations in map view show a number of clearly defined clusters (Figure 2). In some cases, such as south of Fentale the clusters are aligned rift-parallel. In other cases, such as on the border faults, the events are clustered in a less narrow alignment (Figure 2). Based on the spatial distribution, four main clusters are observed that include the majority (1265) of the 1515 earthquakes. Cluster 1 is south-west of the DVC and includes 76 events, cluster 2 includes 171 events and is located on the south-east side of the DVC, cluster 3 includes 179 events and is on the northern side of Fentale volcano, and cluster 4 at the Ankober border has 839 events (Figure 2). In section view, the majority of earthquakes are located at 5–15 km depth. However, the clusters have a diffuse shape without a clearly defined subsurface cross sectional alignment. In addition, earthquake depths are somewhat influenced by the velocity model as shown from the clustering of some earthquakes along horizontal planes that correspond to the velocity model layer boundaries (Figure 2).

Then, the seismic moment was computed for earthquakes beneath the rift as a whole, separately for clusters 1 to 3, and then also the border fault (cluster 4). For the events located in the rift the seismic moment release is 13.26×10^{14} Nm (Figure 6a). The pattern of seismic moment release is not continuous but rather occurs in steps. The plots for cluster 1 to 3 (Figures 6c–6e) shows that the sharpest steps in moment release commonly correspond to occurrences of larger magnitude ($M \geq 3$) earthquakes (e.g., clusters 1 and 3 in particular). However, the histogram of numbers of earthquakes per month coupled with the changes in slope of cumulative number of earthquakes shows that the occurrence of the larger earthquakes are commonly associated with an increase in seismicity rate. This corresponding increase in seismic moment release is less sharp than from an individual

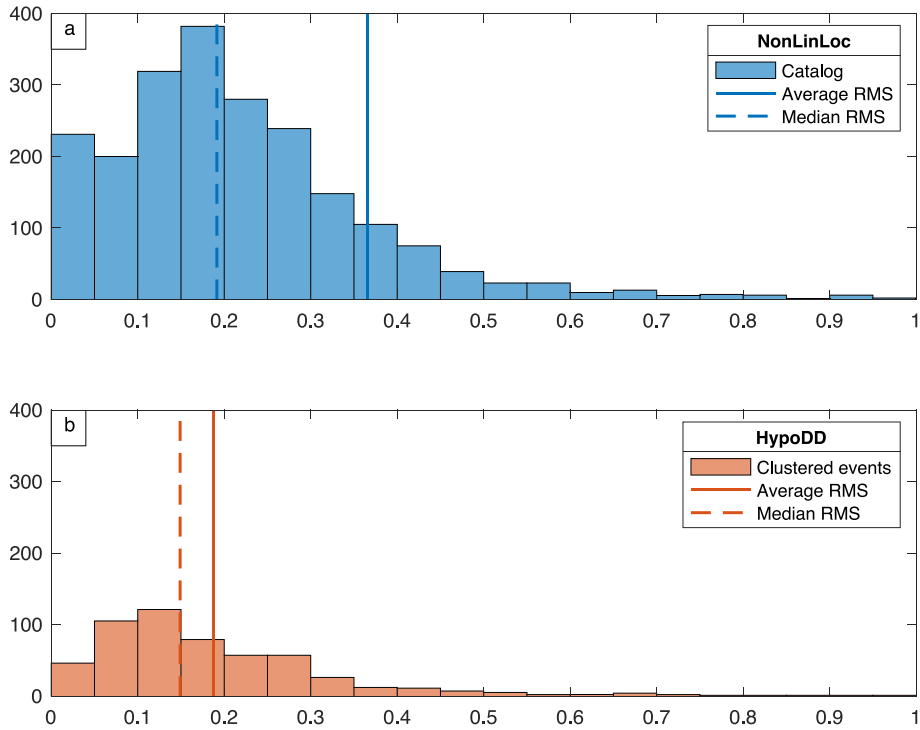

Figure 5. (a) RMS—Number of events histogram for the NonLinLoc catalog. The average of RMS is 0.37 s (solid line) and the median of RMS is 0.19 s (dashed line). (b) RMS—Number of events histogram for the events belonging to the clusters relocalized with HypoDD. In this case, the average of RMS is 0.19 s (solid line) and the median of RMS is 0.15 s (dashed line).

earthquake, but in places still significant. Earthquake activity is therefore rather episodic with bursts of seismicity during which both rate and magnitude of earthquakes increase. For the events localized on the border faults the release of seismic moment is equal to 3.485×10^{15} Nm (Figure 6b), more than double that of the rift. $M \geq 3$ earthquakes are more numerous beneath the border fault than the rift (Figure 6a). The seismic moment computed is negligible when compared to the geodetic moment in the MER, which is four degrees of magnitude greater over the same time period (Déprez et al., 2013). This suggests that most of the earthquakes occur on preexisting seismic structures, as proposed by Greenfield et al. (2019a).

5.2. Waveform Cross Correlation

For each pair of earthquakes recorded in each station, we performed the cross-correlation analysis. Given that the correlograms obtained from this analysis are numerous, here, based on clusters and station distribution, only the most representative correlograms are shown (additional correlograms and dendrograms are shown in the Supporting Information S1).

5.2.1. Cluster 1

For cluster 1, the correlogram shown is obtained from GTFE station (Figure 7a). It is not the nearest station to the cluster, but it includes more waveforms (71) from cluster 1 than the other stations. The time period of the cluster is from 15 November 2001 to 14 February 2002. Three main families are recognizable in this correlogram. The first family occurred from the 15 November and lasted for two days. It is characterized by events highly similar half-way through the swarm, preceded and followed by less similar events. The second family of correlated events occurred from 29 November for one day. In this case, the events are similar at the beginning of the swarm and gradually become less similar through time. The last family of correlated events started from 30 January 2002 for one day, and in this case no characteristic behavior is evident.

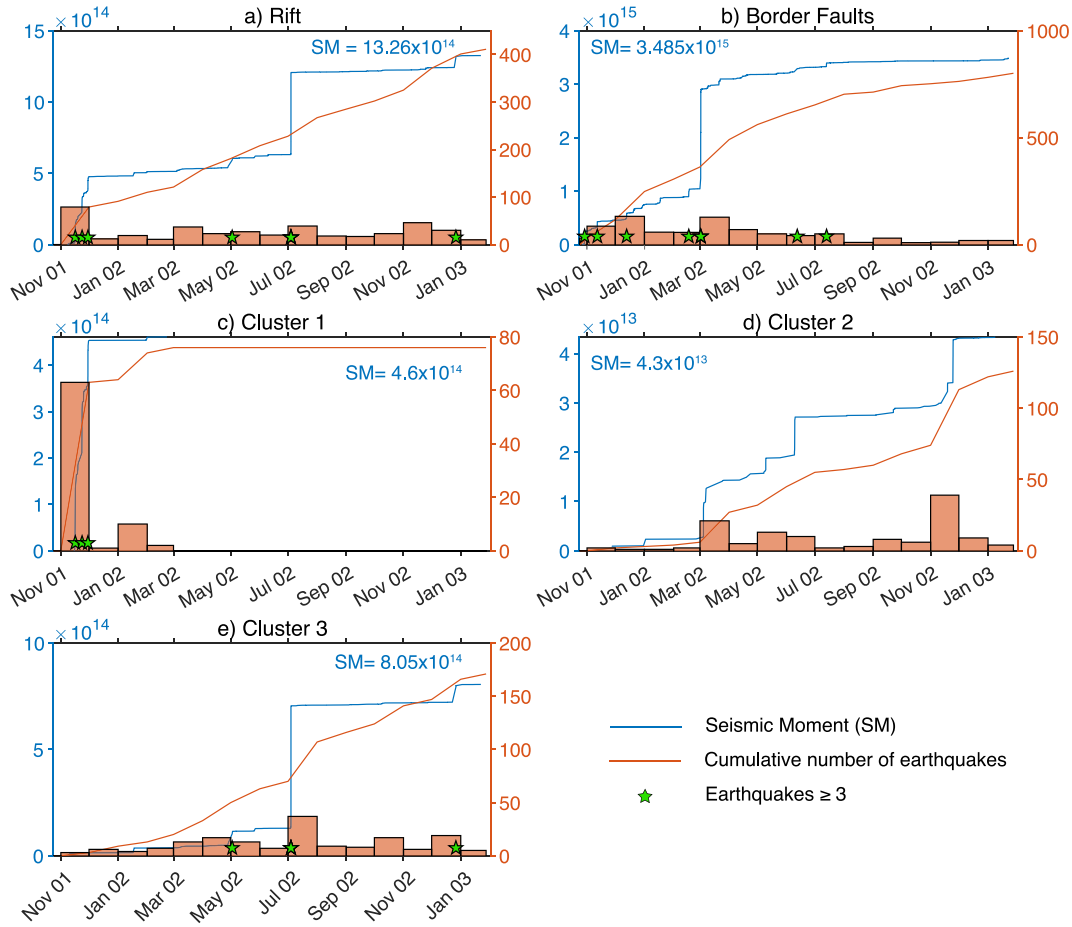

Figure 6. Estimation of seismic moment released by (a) rift, (b) border faults, (c) cluster 1, (d) cluster 2, and (e) cluster 3. The green stars indicate the earthquakes $M \geq 3$. The width of the bins of histograms is 1 month.

5.2.2. Cluster 2

The cluster 2 is located close to MELE station, so the correlogram is obtained from 150 waveforms from this station recorded from 27 November 2001 to 8 January 2003 (Figure 7b). In this correlogram, the first family starts 4 March 2002 for 22 days until 18 March 2002, characterized by similar earthquakes at the beginning of the swarm that gradually became less similar through time. It is followed by one little family with the same behavior. Then, two larger families are found, one with a pattern of reducing waveform similarity through time that started 8 May 2002 and lasted for two days, and another without a clear characteristic behavior that started 9 June 2002 and lasted for two days. In the end, a largest family occurred from 24 November 2002 and lasted for forty-five days until 8 January 2003.

5.2.3. Cluster 3

The nearest station to cluster 3 is the GTFE station, which includes 126 waveforms from earthquakes that occurred from 8 November 2001 to 26 December 2002 (Figure 7c). The correlogram for this cluster shows that the biggest family occurred from 3 July lasted for three days, until 5 July 2002. Thereafter, there are two little families of similar earthquakes, and one final family on 26th December 2002 characterized by seven events that gradually become more similar through time.

5.2.4. Cluster 4

The cluster 4 is located on the border faults, near ANKE station. So, for this cluster, ANKE station is shown. This station has 509 waveforms recorded from 26 October 2001 to 18 January 2003 belonging to cluster 4 (Figure 7d). This correlogram included more earthquakes than for the other clusters (509 earthquakes, compared to the 126 of cluster 3, 150 of cluster 2, and 71 for cluster 1). This makes the visual interpretation of the correlogram more

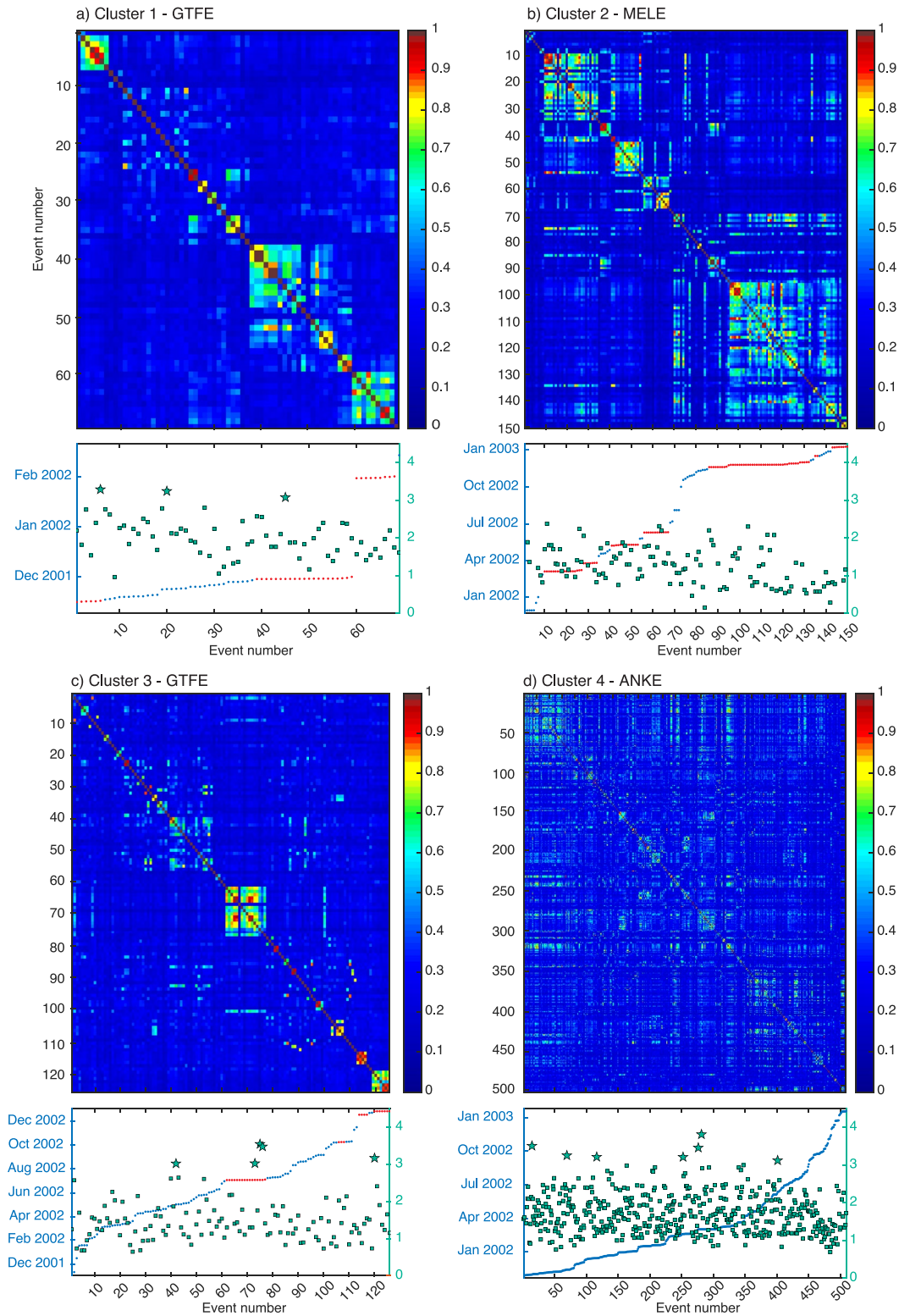

Figure 7.

Table 1
Data Used by HypoDD to Relocate the Earthquakes

	Number of earthquakes	P arrival times	S arrival times	ΔP times	Number of subcluster	Earthquakes in subcluster
Cluster 1	71	3564	3080	428	1	71
Cluster 2	150	1722	1222	300	1	150
Cluster 3	126	4357	3216	390	4	70, 8, 3, 2
Cluster 4	509	38842	26615	16816	6	535, 16, 2, 2, 2, 2

Note. The first column indicates the number of earthquakes of each cluster. The second and the third columns indicate the P and S arrival times in the catalog. The fourth column indicates the number of the P delay times between pair of earthquakes form cross correlation used for the new location. The fifth column indicate the number of subcluster created by HypoDD. In the end, the last column indicates the number of earthquakes in each subcluster.

complex. However despite this, it is evident that the presence of clearly separate families of similar earthquakes is less evident with respect to the clusters in the rift 1–3. In cluster 4, the families of similar earthquakes are composed of very few earthquakes, and within these small groupings, the high cross correlation coefficient seen between pairs of events (red color) infrequent. Therefore overall, there is less evidence for distinct and major earthquake families, and even when minor groups of similar earthquakes occur, their waveforms are only of moderate similarity.

5.3. Relative Earthquake Relocation

With the double difference method in HypoDD the accuracy of earthquake location is improved. The literature is rich with examples of the application of this method to improve the location, as in Waldhauser and Ellsworth (2000), Gambino et al. (2004), Hauksson and Shearer (2005), Mahesh et al. (2012), and Lanza et al. (2022). The new relocation was performed by adding the cross correlation P delay time between pairs of earthquakes (Figure 4) to the catalog derived P- and S- arrival time lags to relocate each cluster separately (Table 1). To apply this method, only the lag time between pairs of earthquakes with a cross correlation coefficient ≥0.7 were used. The new location is shown in Figure 8 in map and Figure 9 in sections (other sections are available in Supporting Information S1). Broadly, the majority of the seismicity is in the upper to middle crust, mostly shallower than 15 km. However, earthquakes in the top 5 km are rare. The main noticeable variation in earthquake depth is that seismicity shallows with proximity to main volcanic centers, a pattern particularly evident near Fentale (Supporting Information S1—cluster 3—EE′ section). The earthquake relocations clearly image discrete seismogenic structures. The major patterns identifiable are that all the clusters tightly align with a NNE strike, parallel to the dominant rift parallel Wonji Fault Belt. However, in detail, cluster 1 (Figure 9—AA′ and BB′ sections) shows two main alignments distinguishable, consistent with E/ENE dipping planes with 5–7 km length. Cluster 2 (Figure 9—CC′ and DD′ sections) shows that the seismically active structure is a ∼8-km-long, *W* – NW dipping plane which projects upward to the surface expression of a normal fault as indicated by the clear topography step visible at the surface. Cluster 3 (Supporting Information S1—EE′ and FF′ sections) shows a decrease of event depths with proximity to Fentale volcano. Cluster 4 (Figure 9 - HH′ - GG′ sections) shows that the seismicity focuses on a clear ∼10-km-long, W-dipping plane.

6. Discussion

The combination of earthquake relocations, waveform cross correlation, and temporal evolution of moment release can be used to probe the space time variability of seismicity in order to better understand driving processes. A major outcome of this investigation is that for the majority of clusters, especially in the rift, the earthquakes do not occur in a steady and continuous manner but instead in episodic bursts of earthquake that range from 1/2 days to 45 days long during which the numbers of earthquakes and seismic moment release increases significantly

Figure 7. Cross correlograms for cluster 1, cluster 2, cluster 3, and cluster 4. In the correlograms, the axes are the same and show the events sorted by time. Each pair of events is represented by a pixel, with a color that can range from blue, for low correlation coefficient (0), to red for high correlation coefficient (1). The diagonal of the diagram presents the maximum correlation coefficient because it is the comparison of earthquakes with themselves (auto-correlation). And the diagram is a mirror image of itself with respect to the diagonal. The correlograms of the different clusters include a different number of waveforms: 71 for cluster 1, 150 for cluster 2, 126 for cluster 3, and 509 for cluster 4. The blue color indicates a low degree of similarity while green, yellow, and red colors indicate high degree of similarity. Below each correlogram there is a plot with earthquakes number versus earthquakes date, these plots showcase the occurrence of earthquakes in time yet using the same *x*-axis as the correlogram. Flat sections (in red) are periods with high seismic rate. On the left *y*-axes there are the date of earthquake occurrence, on the right *y*-axes there are the magnitudes of the earthquakes.

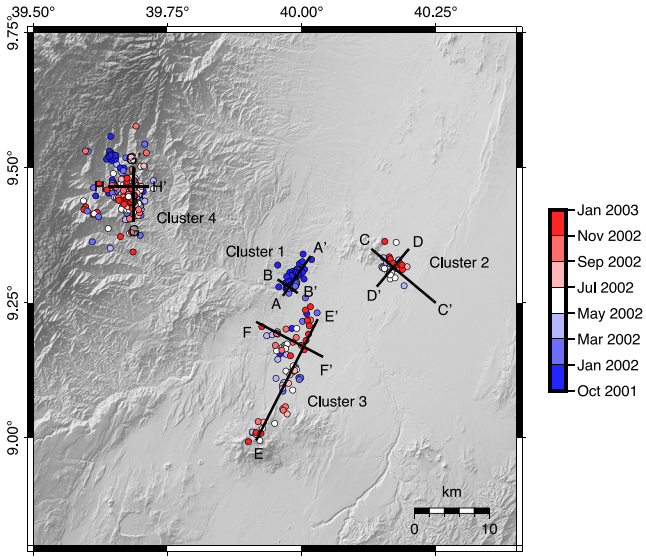

Figure 8. Seismicity relocated with HypoDD using the catalog data and the differential times between new picked P arrivals computed in the cross-correlation analysis. Each cluster was relocated individually but all the earthquakes are colored based on time occurrence (in blue are the oldest and in red the more recent). The black solid lines represent the cross sections, which for the clusters 1, 2, and 4 are shown in Figure 9. The sections of the cluster 3 are in the Supporting Information S1.

(Figures 6 and 7). The distribution of earthquakes magnitudes in the families reveals that the occurrence of the biggest earthquakes is randomly distributed in time and that usually the families do not start with a main shock. This can be explained with an increase of fluid pressure due to fluid migration (Bachmann et al., 2012).

The cross correlation analysis allows us to identify families of similar earthquakes in a seismic swarm. The results of cross correlation analysis show that all of the three clusters localized in the rift (cluster 1, cluster 2, and cluster 3) are characterized by the presence of families of similar earthquakes (Figure 7). The correlograms also show that the event families for these three clusters occur within restricted time periods in which successive earthquakes are within the same discrete family. In other words, the seismicity is characterized by the background occurrence of nonsimilar earthquakes, but interspersed with short lived, discrete swarms of earthquakes that are highly self-similar. Short lived swarms of highly self-similar earthquakes are highly typical of fluid induced seismicity, in which local restrictions or barriers to fluid flow locally increase the stressing rate and induce earthquakes (Rowland & Sibson, 2004). Since the position of the restriction or barrier is fixed, this provides a mechanism to continuously stress the same position along the fault zone and produce swarms of earthquakes with the same location and focal mechanism. In addition, fluids affect the frictional fault mechanics, generally making it easier for the fault to slip (Sibson, 2000), potentially aseismically where there are no restrictions to fluid flow.

In addition, the families of highly correlated earthquakes in the correlograms of the clusters in the rift show more details. Specifically, most of the families show a pattern of (a) the start of the swarm has highly similar earthquakes,

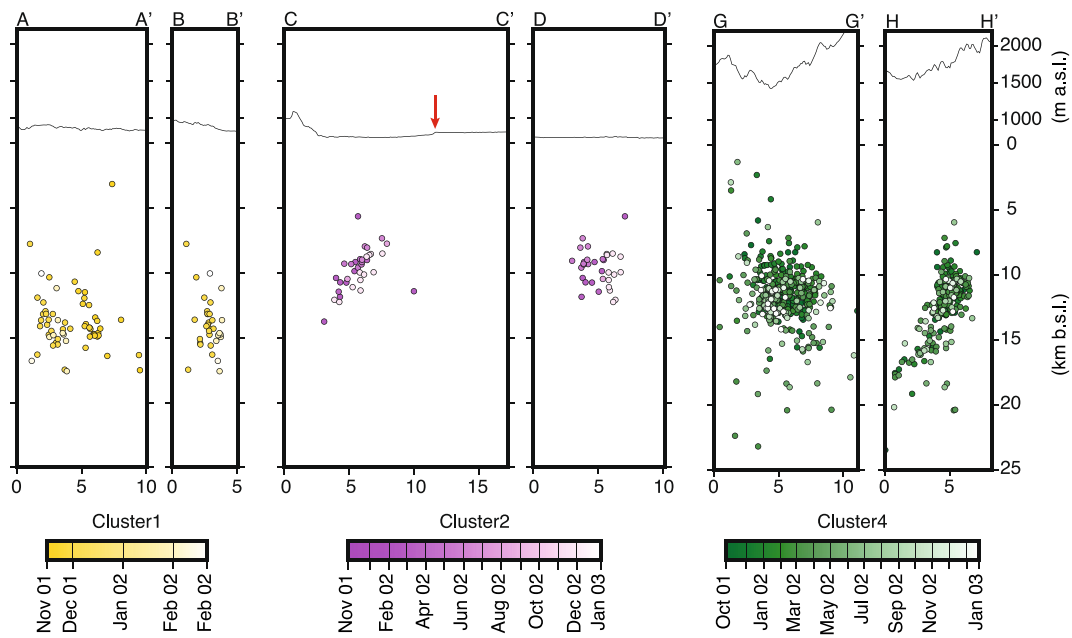

Figure 9. Sections of seismicity relocated using the catalog and the cross correlation data. The positions of the sections are reported in Figure 8. Here are shown A-A′ and B-B′ (cluster 1), C-C′ and D-D′ (cluster 2), and G-G′ and H-H′ (cluster 4) sections. The sections of cluster 3 (E-E′ and F-F′) are shown in the Supporting Information S1. Each section has a color bar based on the time of earthquake occurrence of the cluster. Cluster 1 started on 15 November 2001 and finished on 22 February 2002. Cluster 2 began on 27 November 2001 until January 2003. Cluster 4 is the longest and began on 25 October 2001 until 23 January 2003. The red arrow in section C-C′ indicates the step on the topography.

and the degree of similarity then progressively decreases through time, or (b) that the peak in degree of similarity is in the temporal center of the swarm, with similarity progressively decreasing both before and after this central peak. Both patterns are tentative evidence for an element of a small but coherent and progressive spatial migration of earthquakes through time, or alternatively a small but coherent change in earthquake focal mechanism through time from a fixed source. Such a pattern is also common for fluid induced earthquakes, in which, for example, local restrictions to fluid flow may have a significant length scale with bursts of fluid flow inducing earthquakes along a plane rather than a discrete point (Cox, 2010). This contrasts the dominant pattern in cluster 4 on the rift valley border fault in which the majority of earthquakes do not show a high degree of similarity. This potentially indicates a reduced role of fluid migration in inducing the seismicity, and that instead, tectonic processes such as microseismic creep along a fault system may be releasing stress.

A primary outcome of the higher resolution earthquake locations from HypoDD is that the majority of earthquake clusters compact to NNE striking, steeply dipping (more than 60°) planes that commonly correlate to the surface expression of normal faults (e.g., Figure 9-CC′ section). The interpretation of them being normal faults is supported by the dominant focal mechanism of the seismicity identified in previous studies (Keir et al., 2006). The combination of new high resolution earthquake locations combined with the interpretation of the correlogram content is important since it provides direct evidence that seismicity is likely driven by fluid flow and that this is concentrated on existing and major within-rift faults. This interpretation is also further supported by the low seismic moment release, since activation of preexisting structures requires less stress to make a fault slip compared to undeformed conditions (Yamashita & Tsutsumi, 2018).

The depth range of most of the seismicity (5–15 km) suggests that the source of the fluid is not linked to the shallow (<5 km-deep) meteoric driven hydrothermal system. This is supported by the lack of spatial correlation between our seismic catalog and the surface distribution of active and fossil hydrothermal features (Raggiunti et al., 2021). The depth of our fluid induced seismicity is instead more likely to be related to fluid migration from below, as has been interpreted in a number of other continental rifts. For example, Reyners et al. (2007) interpret the upper-crustal seismicity recorded in the southwestern termination of the Taupo Volcanic Zone (New Zealand) to be promoted by fluids exsolved from magma intrusions cooling in the lower crust. In East Africa, Lindenfeld et al. (2012) observed earthquake swarms interpreted to be caused by crustal fluid migrations and/or CO_2 emanations rising from a magmatic body located in the upper crust. In some areas of East Africa, anomalous lower crustal earthquakes have also been observed and linked to mantle derived CO_2 migrating along preexisting and deep penetrating faults (La Rosa et al., 2021; Lee et al., 2016; Muluneh et al., 2020). In contrast, very high density seismic experiments localized at active volcanoes in the MER have shown strong evidence for <5 km deep, low magnitude (M < 1.5) microseismicity strongly associated with surface hydrothermal systems with fluids likely being the meteoric derived H_2O (Greenfield et al., 2019a; Lavayssière, Greenfield, et al., 2019; Wilks et al., 2017). Together, this provides evidence for mantle derived fluid migration through the crust guided by rift valley faults, superimposed on which are the shallow (<5 km) hydrothermal systems mainly localized to volcanic systems.

The lack of discrete earthquake families for cluster 4 on the Ankober border fault provides evidence that seismicity on the border fault is not strongly related to fluid migration but is instead more likely stress-driven. The earthquake cluster defines a clear steep (~60°), NW dipping plane and therefore points toward it being an antithetic fault. The lack of fluid involvement is supported by the lack of hydrothermal features (e.g., hot springs, fumaroles) at the surface in this region (Keir et al., 2009). However, observations of deep earthquake swarms and elevated surface CO_2 flux elsewhere in East Africa (Lee et al., 2016), suggest that rift border faults can sometimes also be important deep sourced fluid conduits. However, our study shows that within-rift faults are also important for this process.

7. Conclusions

In this work, we conducted the earthquake relocation in the northern MER using waveform cross correlation coupled with a detailed appraisal of the temporal pattern of seismicity in order to better understand driving mechanisms of seismicity during magmatic rifting. Seismicity mainly occurs in discrete clusters within the rift and at the rift border fault. Within the rift, the seismicity in the clusters occurs in a number of day-to month-long swarms of similar earthquakes during which seismicity rate and earthquake magnitude increases, which we interpret as fluid induced seismicity. In contrast, seismicity on the border fault occurs in a more continuous fashion with a

lack of waveform similarity, which we interpret as likely stress-driven microseismic creep. High resolution earthquake relocation using a double-difference location method performed with HypoDD found that they are localized mainly between 5 and 15 km depth with earthquake cluster showing clear alignment to *N*–NNE striking, ~60° dipping planes that commonly project to the surface positions of rift normal faults. The earthquake relocations coupled with analysis of release of seismic moment and cross correlation show that the fluid migration that we interpret to be responsible for most of the within-rift seismicity is localized to the rift valley faults, with depth of earthquakes suggesting a deeper, probably mantle, source to the fluids. Our results show that within-rift fluid migration is likely an important driver of fault slip in magma rich continental rifts.

Data Availability Statement

The original earthquake catalog is presented in Keir et al. (2006) and it is available in Data Set S2. All seismic data were downloaded through the IRIS Data Management Center (https://www.fdsn.org/networks/), including the following seismic networks: (a) XJ: Ethiopian Afar Geophysical Lithospheric Experiment (https://www.fdsn.org/networks/detail/XJ_2002/); (b) XM: Ethiopia-Afar Geoscientific Lithospheric Experiment 6TD Passive Array (https://www.fdsn.org/networks/detail/XM_2002/); and (c) YJ: Ethiopia-Afar Geoscientific Lithospheric Experiment (https://www.fdsn.org/networks/detail/YJ_2001/). The velocity model used in NonNinLoc was proposed by Maguire et al. (2006). Generic Mapping Tools (GMT; Wessel et al., 2013) was used to make the figures. For the cross-correlation analysis, we used GISMO, a seismic data analysis toolbox for MATLAB by Thompson et al. (2017), available at: http://geoscience-community-codes.github.io/GISMO/. Accessed:Feb11,2020.http://doi.org/10.5281/zenodo.1404723 http://doi.org/10.5281/zenodo.1404723. For the high resolution location, we used HypoDD, a program to compute double-difference hypocenter locations, by Waldhauser and Ellsworth (2000).

Acknowledgments
MR., DK., and CP. are funded by 2017 PRIN project—protocol MIUR: 2017P9AT72 PE10. DK is also supported by Natural Environment Research Council under NERC Grant NE/L013932/1. M.R. was also supported by PhD studentship from University of Pisa.

References

Abebe, B., Acocella, V., Korme, T., & Ayalew, D. (2007). Quaternary faulting and volcanism in the Main Ethiopian Rift. *Journal of African Earth Sciences*, *48*(2–3), 115–124. https://doi.org/10.1016/j.jafrearsci.2006.10.005

Agostini, A., Bonini, M., Corti, G., Sani, F., & Mazzarini, F. (2011). Fault architecture in the Main Ethiopian Rift and comparison with experimental models: Implications for rift evolution and Nubia–Somalia kinematics. *Earth and Planetary Science Letters*, *301*(3–4), 479–492. https://doi.org/10.1016/j.epsl.2010.11.024

Ayele, A. (1995). *Earthquake catalogue of the horn of Africa for the period 1960–1993*. Seismological Department—Uppsala University.

Ayele, A., & Kulhánek, O. (1997). Spatial and temporal variations of seismicity in the Horn of Africa from 1960 to 1993. *Geophysical Journal International*, *130*(3), 805–810. https://doi.org/10.1111/j.1365-246x.1997.tb01875.x

Bachmann, C. E., Wiemer, S., Goertz-Allmann, B., & Woessner, J. (2012). Influence of pore-pressure on the event-size distribution of induced earthquakes. *Geophysical Research Letters*, *39*(9). https://doi.org/10.1029/2012gl051480

Birhanu, Y., Bendick, R., Fisseha, S., Lewi, E., Floyd, M., King, R., & Reilinger, R. (2016). GPS constraints on broad scale extension in the Ethiopian Highlands and Main Ethiopian Rift. *Geophysical Research Letters*, *43*(13), 6844–6851. https://doi.org/10.1002/2016gl069890

Boccaletti, M., Mazzuoli, R., Bonini, M., Trua, T., & Abebe, B. (1999). Plio-quaternary volcanotectonic activity in the northern sector of the MAIN EOPIAN Rift: Relationships with oblique rifting. *Journal of African Earth Sciences*, *29*(4), 679–698. https://doi.org/10.1016/s0899-5362(99)00124-4

Bonini, M., Corti, G., Innocenti, F., Manetti, P., Mazzarini, F., Abebe, T., & Pecskay, Z. (2005). Evolution of the Main Ethiopian Rift in the frame of Afar and Kenya rifts propagation. *Tectonics*, *24*(1). https://doi.org/10.1029/2004tc001680

Bormann, P., Baumbach, M., Bock, M., Grosser, H., Choy, G. L., & Boatwright, J. (2002). Seismic sources and source parameters. In P. Bormann (Ed.), *IASPEI new manual seismological observatory practice*, *GeoForschungsZentrum Potsdam* (Vol. 1, pp. 411–427). Chapter 3, 94.

Brune, S., Williams, S. E., & Müller, R. D. (2017). Potential links between continental rifting, CO_2 degassing and climate change through time. *Nature Geoscience*, *10*(12), 941–946. https://doi.org/10.1038/s41561-017-0003-6

Campillo, M., & Roux, P. (2015). Crust and lithospheric structure-seismic imaging and monitoring with ambient noise correlations.

Casey, M., Ebinger, C., Keir, D., Gloaguen, R., & Mohamed, F. (2006). Strain accommodation in transitional rifts: Extension by magma intrusion and faulting in Ethiopian rift magmatic segments. *Geological Society, London, Special Publications*, *259*(1), 143–163. https://doi.org/10.1144/gsl.sp.2006.259.01.13

Chorowicz, J. (2005). The east African rift system. *Journal of African Earth Sciences*, *43*(1–3), 379–410. https://doi.org/10.1016/j.jafrearsci.2005.07.019

Christensen, N. I. (1984). Pore pressure and oceanic crustal seismic structure. *Geophysical Journal International*, *79*(2), 411–423. https://doi.org/10.1111/j.1365-246x.1984.tb02232.x

Chu, D., & Gordon, R. G. (1999). Evidence for motion between nubia and Somalia along the southwest Indian ridge. *Nature*, *398*(6722), 64–67. https://doi.org/10.1038/18014

Corti, G. (2009). Continental rift evolution: From rift initiation to incipient break-up in the Main Ethiopian Rift, East Africa. *Earth-Science Reviews*, *96*(1–2), 1–53. https://doi.org/10.1016/j.earscirev.2009.06.005

Corti, G., Sani, F., Florio, A. A., Greenfield, T., Keir, D., Erbello, A., et al. (2020). Tectonics of the Asela-Langano margin, Main Ethiopian Rift (East Africa). *Tectonics*, *39*(8), e2020TC006075. https://doi.org/10.1029/2020tc006075

Cox, S. (2010). The application of failure mode diagrams for exploring the roles of fluid pressure and stress states in controlling styles of fracture-controlled permeability enhancement in faults and shear zones. *Geofluids*, *10*(1–2), 217–233. https://doi.org/10.1111/j.1468-8123.2010.00281.x

Deichmann, N. (2006). Local magnitude, a moment revisited. *Bulletin of the Seismological Society of America*, *96*(4A), 1267–1277. https://doi.org/10.1785/0120050115

Déprez, A., Doubre, C., Masson, F., & Ulrich, P. (2013). Seismic and aseismic deformation along the East African rift system from a reanalysis of the GPS velocity field of Africa. *Geophysical Journal International*, *193*(3), 1353–1369. https://doi.org/10.1093/gji/ggt085

Diehl, T., Waldhauser, F., Cochran, J. R., Kamesh Raju, K., Seeber, L., Schaff, D., & Engdahl, E. (2013). Back-arc extension in the Andaman Sea: Tectonic and magmatic processes imaged by high-precision teleseismic double-difference earthquake relocation. *Journal of Geophysical Research: Solid Earth*, *118*(5), 2206–2224. https://doi.org/10.1002/jgrb.50192

Dodge, D., & Walter, W. (2015). Initial global seismic cross-correlation results: Implications for empirical signal detectors. *Bulletin of the Seismological Society of America*, *105*(1), 240–256. https://doi.org/10.1785/0120140166

Ebinger, C., & Casey, M. (2001). Continental breakup in magmatic provinces: An Ethiopian example. *Geology*, *29*(6), 527–530. https://doi.org/10.1130/0091-7613(2001)029<0527:cbimpa>2.0.co;2

Fernandes, R., Ambrosius, B., Noomen, R., Bastos, L., Combrinck, L., Miranda, J., & Spakman, W. (2004). Angular velocities of Nubia and Somalia from continuous GPS data: Implications on present-day relative kinematics. *Earth and Planetary Science Letters*, *222*(1), 197–208. https://doi.org/10.1016/j.epsl.2004.02.008

Fischer, T., Horálek, J., Hrubcová, P., Vavryčuk, V., Bräuer, K., & Kämpf, H. (2014). Intra-continental earthquake swarms in West-Bohemia and Vogtland: A review. *Tectonophysics*, *611*, 1–27. https://doi.org/10.1016/j.tecto.2013.11.001

Gambino, S., Mostaccio, A., Patanè, D., Scarfì, L., & Ursino, A. (2004). High-precision locations of the microseismicity preceding the 2002–2003 Mt. Etna eruption. *Geophysical Research Letters*, *31*(18), L18604. https://doi.org/10.1029/2004gl020499

Got, J.-L., Fréchet, J., & Klein, F. W. (1994). Deep fault plane geometry inferred from multiplet relative relocation beneath the south flank of Kilauea. *Journal of Geophysical Research*, *99*(B8), 15375–15386. https://doi.org/10.1029/94jb00577

Greenfield, T., Keir, D., Kendall, J.-M., & Ayele, A. (2019a). Low-frequency earthquakes beneath Tullu Moye volcano, Ethiopia, reveal fluid pulses from shallow magma chamber. *Earth and Planetary Science Letters*, *526*, 115782. https://doi.org/10.1016/j.epsl.2019.115782

Greenfield, T., Keir, D., Kendall, J.-M., & Ayele, A. (2019b). Seismicity of the Bora-Tullu Moye volcanic field, 2016–2017. *Geochemistry, Geophysics, Geosystems*, *20*(2), 548–570. https://doi.org/10.1029/2018gc007648

Hauksson, E., & Shearer, P. (2005). Southern California hypocenter relocation with waveform cross-correlation, part 1: Results using the double-difference method. *Bulletin of the Seismological Society of America*, *95*(3), 896–903. https://doi.org/10.1785/0120040167

Hickman, S., Sibson, R., & Bruhn, R. (1995). Introduction to special section: Mechanical involvement of fluids in faulting. *Journal of Geophysical Research*, *100*(B7), 12831–12840. https://doi.org/10.1029/95jb01121

Hofstetter, R., & Beyth, M. (2003). The Afar depression: Interpretation of the 1960–2000 earthquakes. *Geophysical Journal International*, *155*(2), 715–732. https://doi.org/10.1046/j.1365-246x.2003.02080.x

Keir, D., Bastow, I. D., Corti, G., Mazzarini, F., & Rooney, T. O. (2015). The origin of along-rift variations in faulting and magmatism in the Ethiopian Rift. *Tectonics*, *34*(3), 464–477. https://doi.org/10.1002/2014tc003698

Keir, D., Bastow, I. D., Whaler, K. A., Daly, E., Cornwell, D. G., & Hautot, S. (2009). Lower crustal earthquakes near the Ethiopian Rift induced by magmatic processes. *Geochemistry, Geophysics, Geosystems*, *10*(6), Q0AB02. https://doi.org/10.1029/2009gc002382

Keir, D., Ebinger, C., Stuart, G., Daly, E., & Ayele, A. (2006). Strain accommodation by magmatism and faulting as rifting proceeds to breakup: Seismicity of the northern Ethiopian Rift. *Journal of Geophysical Research*, *111*(B5), B05314. https://doi.org/10.1029/2005jb003748

Keranen, K., & Klemperer, S. (2008). Discontinuous and diachronous evolution of the Main Ethiopian Rift: Implications for development of continental rifts. *Earth and Planetary Science Letters*, *265*(1–2), 96–111. https://doi.org/10.1016/j.epsl.2007.09.038

Kogan, L., Fisseha, S., Bendick, R., Reilinger, R., McClusky, S., King, R., & Solomon, T. (2012). Lithospheric strength and strain localization in continental extension from observations of the East African Rift. *Journal of Geophysical Research*, *117*(B3), B03402. https://doi.org/10.1029/2011jb008516

Lanza, F., Roman, D. C., Power, J. A., Thurber, C. H., & Hudson, T. (2022). Complex magmatic-tectonic interactions during the 2020 Makushin Volcano, Alaska, earthquake swarm. *Earth and Planetary Science Letters*, *587*, 117538. https://doi.org/10.1016/j.epsl.2022.117538

La Rosa, A., Keir, D., Doubre, C., Sani, F., Corti, G., Leroy, S., et al. (2021). Lower crustal earthquakes in the March 2018 sequence along the Western Margin of Afar. *Geochemistry, Geophysics, Geosystems*, *22*(4), e2020GC009614. https://doi.org/10.1029/2020gc009614

Lavayssière, A., Drooff, C., Ebinger, C., Gallacher, R., Illsley-Kemp, F., Oliva, S. J., & Keir, D. (2019). Depth extent and kinematics of faulting in the southern Tanganyika rift, Africa. *Tectonics*, *38*(3), 842–862. https://doi.org/10.1029/2018tc005379

Lavayssière, A., Greenfield, T., Keir, D., Ayele, A., & Kendall, J.-M. (2019). Local seismicity near the actively deforming Corbetti volcano in the Main Ethiopian Rift. *Journal of Volcanology and Geothermal Research*, *381*, 227–237. https://doi.org/10.1016/j.jvolgeores.2019.06.008

Lee, H., Muirhead, J. D., Fischer, T. P., Ebinger, C. J., Kattenhorn, S. A., Sharp, Z. D., & Kianji, G. (2016). Massive and prolonged deep carbon emissions associated with continental rifting. *Nature Geoscience*, *9*(2), 145–149. https://doi.org/10.1038/ngeo2622

Lindenfeld, M., Rümpker, G., Link, K., Koehn, D., & Batte, A. (2012). Fluid-triggered earthquake swarms in the Rwenzori region, East African rift—Evidence for rift initiation. *Tectonophysics*, *566*, 95–104. https://doi.org/10.1016/j.tecto.2012.07.010

Lomax, A. (2008). *The Nonlinloc software guide*. ALomax Scientific. Retrieved from http://alomax.free.fr/nlloc

Lomax, A., Michelini, A., Curtis, A., & Meyers, R. (2009). Earthquake location, direct, global-search methods. *Encyclopedia of complexity and systems science*, *5*, 2449–2473.

Lomax, A., Virieux, J., Volant, P., & Berge-Thierry, C. (2000). Probabilistic earthquake location in 3D and layered models. In *Advances in seismic event location* (pp. 101–134). Springer.

Mackenzie, G., Thybo, H., & Maguire, P. (2005). Crustal velocity structure across the Main Ethiopian Rift: Results from two-dimensional wide-angle seismic modelling. *Geophysical Journal International*, *162*(3), 994–1006. https://doi.org/10.1111/j.1365-246x.2005.02710.x

Maestrelli, D., Corti, G., Bonini, M., Montanari, D., & Sani, F. (2021). Caldera collapse and tectonics along the Main Ethiopian Rift: Reviewing possible relationships. *Comptes Rendus Geoscience*, *353*(S2), 1–19. https://doi.org/10.5802/crgeos.63

Maguire, P. (2001). A new dimension for UK seismology. *Astronomy and Geophysics*, *42*(6), 6–23. https://doi.org/10.1046/j.1468-4004.2001.42623.x

Maguire, P., Ebinger, C., Stuart, G., Mackenzie, G., Whaler, K., Kendall, J.-M., et al. (2003). Geophysical project in Ethiopia studies continental breakup. *EOS, Transactions American Geophysical Union*, *84*(35), 337–343. https://doi.org/10.1029/2003eo350002

Maguire, P., Keller, G., Klemperer, S., Mackenzie, G., Keranen, K., Harder, S., et al. (2006). Crustal structure of the northern Main Ethiopian Rift from the EAGLE controlled-source survey; a snapshot of incipient lithospheric break-up. *Geological Society, London, Special Publications*, *259*(1), 269–292. https://doi.org/10.1144/gsl.sp.2006.259.01.21

Mahesh, P., Gupta, S., Rai, S., & Sarma, P. R. (2012). Fluid driven earthquakes in the Chamoli Region, Garhwal Himalaya: Evidence from local earthquake tomography. *Geophysical Journal International*, *191*(3), 1295–1304. https://doi.org/10.1111/j.1365-246x.2012.05672.x

Mohr, P., & Gouin, P. (1976). The Ethiopian rift system. *Bull. Geophys. Obs. Addis Ababa*, *11*.

Muluneh, A. A., Brune, S., Illsley-Kemp, F., Corti, G., Keir, D., Glerum, A., et al. (2020). Mechanism for deep crustal seismicity: Insight from modeling of deformation processes at the Main Ethiopian Rift. *Geochemistry, Geophysics, Geosystems*, *21*(7), e2020GC008935. https://doi.org/10.1029/2020gc008935

Pürschel, M., Gloaguen, R., & Stadler, S. (2013). Geothermal activities in the Main Ethiopian Rift: Hydrogeochemical characterization of geothermal waters and geothermometry applications (Dofan-Fantale, Gergede-Sodere, Aluto-Langano). *Geothermics*, *47*, 1–12. https://doi.org/10.1016/j.geothermics.2013.01.001

Raggiunti, M., Keir, D., & Pagli, C. (2021). Mapping hydrothermal alteration at the Fentale-Dofan magmatic segment of the Main Ethiopian Rift. *Frontiers of Earth Science*, *9*, 712. https://doi.org/10.3389/feart.2021.716144

Reyners, M., Eberhart-Phillips, D., & Stuart, G. (2007). The role of fluids in lower-crustal earthquakes near continental rifts. *Nature*, *446*(7139), 1075–1078. https://doi.org/10.1038/nature05743

Rowland, J., & Sibson, R. (2004). Structural controls on hydrothermal flow in a segmented rift system, Taupo Volcanic Zone, New Zealand. *Geofluids*, *4*(4), 259–283. https://doi.org/10.1111/j.1468-8123.2004.00091.x

Ruch, J., Keir, D., Passarelli, L., Di Giacomo, D., Ogubazghi, G., & Jónsson, S. (2021). Revealing 60 years of earthquake swarms in the southern red sea, Afar and the Gulf of Aden. *Frontiers of Earth Science*, *9*. https://doi.org/10.3389/feart.2021.664673

Saccorotti, G., Bruni, R., Bonini, M., Corti, G., Keir, D., & Sani, F. (2022). Recent seismic sequences and activation of normal fault systems in the Mugello basin and surrounding areas (northern Apennines, Italy). *Frontiers of Earth Science*, *646*. https://doi.org/10.3389/feart.2022.879160

Schaff, D. P. (2008). Semiempirical statistics of correlation-detector performance. *Bulletin of the Seismological Society of America*, *98*(3), 1495–1507. https://doi.org/10.1785/0120060263

Schaff, D. P., Richards, P. G., Slinkard, M., Heck, S., & Young, C. (2018). Lg-wave cross correlation and Epicentral double-difference location in and near China. *Bulletin of the Seismological Society of America*, *108*(3A), 1326–1345. https://doi.org/10.1785/0120170137

Shcherbakov, R., Turcotte, D. L., & Rundle, J. B. (2004). A generalized Omori's law for earthquake aftershock decay. *Geophysical Research Letters*, *31*(11), L11613. https://doi.org/10.1029/2004gl019808

Sibson, R. H. (2000). Fluid involvement in normal faulting. *Journal of Geodynamics*, *29*(3–5), 469–499. https://doi.org/10.1016/s0264-3707(99)00042-3

Siegburg, M., Bull, J. M., Nixon, C. W., Keir, D., Gernon, T. M., Corti, G., et al. (2020). Quantitative constraints on faulting and fault slip rates in the northern Main Ethiopian Rift. *Tectonics*, *39*(8), e2019TC006046. https://doi.org/10.1029/2019tc006046

Teklemariam, M., & Kebede, S. (2010). Strategy for geothermal resource exploration and development in Ethiopia. In *Proceedings world geothermal congress* (pp. 25–30).

Temtime, T., Biggs, J., Lewi, E., & Ayele, A. (2020). Evidence for active rhyolitic dike intrusion in the northern Main Ethiopian Rift from the 2015 fentale seismic swarm. *Geochemistry, Geophysics, Geosystems*, *21*(6), e2019GC008550. https://doi.org/10.1029/2019gc008550

Thompson, G., Reyes, C., & Kempler, L. (2017). GISMO: A MATLAB toolbox for seismic research, monitoring, & education. In *2017 AGU fall meeting*. AGU.

Waldhauser, F., & Ellsworth, W. L. (2000). A double-difference earthquake location algorithm: Method and application to the northern Hayward fault, California. *Bulletin of the Seismological Society of America*, *90*(6), 1353–1368. https://doi.org/10.1785/0120000006

Waldhauser, F., & Schaff, D. P. (2008). Large-scale relocation of two decades of northern California seismicity using cross-correlation and double-difference methods. *Journal of Geophysical Research*, *113*(B8), B08311. https://doi.org/10.1029/2007jb005479

Waldhauser, F., Schaff, D. P., Diehl, T., & Engdahl, E. R. (2012). Splay faults imaged by fluid-driven aftershocks of the 2004 M_w 9.2 Sumatra-Andaman earthquake. *Geology*, *40*(3), 243–246. https://doi.org/10.1130/g32420.1

Wessel, P., Smith, W. H., Scharroo, R., Luis, J., & Wobbe, F. (2013). Generic mapping tools: Improved version released. *Eos, Transactions American Geophysical Union*, *94*(45), 409–410.

Wilks, M., Kendall, J.-M., Nowacki, A., Biggs, J., Wookey, J., Birhanu, Y., et al. (2017). Seismicity associated with magmatism, faulting and hydrothermal circulation at Aluto Volcano, Main Ethiopian Rift. *Journal of Volcanology and Geothermal Research*, *340*, 52–67. https://doi.org/10.1016/j.jvolgeores.2017.04.003

Williams, F., Williams, M., & Aumento, F. (2004). Tensional fissures and crustal extension rates in the northern part of the Main Ethiopian Rift. *Journal of African Earth Sciences*, *38*(2), 183–197. https://doi.org/10.1016/j.jafrearsci.2003.10.007

Wolfenden, E., Ebinger, C., Yirgu, G., Deino, A., & Ayalew, D. (2004). Evolution of the northern Main Ethiopian Rift: Birth of a triple junction. *Earth and Planetary Science Letters*, *224*(1–2), 213–228. https://doi.org/10.1016/j.epsl.2004.04.022

Wolfenden, E., Ebinger, C., Yirgu, G., Renne, P. R., & Kelley, S. P. (2005). Evolution of a volcanic rifted margin: Southern Red sea, Ethiopia. *Geological Society of America Bulletin*, *117*(7–8), 846–864. https://doi.org/10.1130/b25516.1

Woods, J., Winder, T., White, R. S., & Brandsdóttir, B. (2019). Evolution of a lateral dike intrusion revealed by relatively-relocated dike-induced earthquakes: The 2014–15 Bárðarbunga–Holuhraun rifting event, Iceland. *Earth and Planetary Science Letters*, *506*, 53–63. https://doi.org/10.1016/j.epsl.2018.10.032

Yamashita, T., & Tsutsumi, A. (2018). *Involvement of fluids in earthquake ruptures* (Vol. 10, pp. 978–984). Springer.